Unraveling the mechanisms of visible light photocatalytic NO purification on earth-abundant insulator-based core-shell heterojunctions

Journal:	*Environmental Science & Technology*
Manuscript ID	es-2017-05457y.R1
Manuscript Type:	Article
Date Submitted by the Author:	n/a
Complete List of Authors:	Wang, Hong; Chongqing Technology and Business University Sun, Yanjuan; Chongqing Technology and Business University, Key Laboratory of Catalysis Science and Technology of Chongqing Education Commissio Jiang, Guangming; zhejiang university, Engineering Research Center for Waste Oil Recovery Technology and Equipment Zhang, Yu Xin; Chongqing University, College of Materials Science and Engneering Huang, Hongwei; China University of Geosciences, School of Materials Science and Technology Wu, Zhongbiao; Zhejiang University, Department of environmental engineering Lee, Shun Cheng; The HongKong Polytechnic University, Department of Civil and Structural Engineering Dong, Fan; Chongqing Technology and Business University, College of Environmental and Biological Engineering, Key laboratory of Catalysis Science and Technology of Chongqing Education Commission

Unraveling the mechanisms of visible light photocatalytic NO purification on earth-abundant insulator-based core-shell heterojunctions

*Hong Wang [†], Yanjuan Sun [†], Guangming Jiang [†], Yuxin Zhang [‡], Hongwei Huang [‖], Zhongbiao Wu [+], S. C. Lee [§], Fan Dong [†,]**

† Chongqing Key Laboratory of Catalysis and New Environmental Materials, College of Environment and Resources, Chongqing Technology and Business University, Chongqing 400067, China.

‡ State Key Laboratory of Mechanical Transmissions, College of Materials Science and Engineering, Chongqing University, Chongqing 400044, People's Republic of China.

‖ Beijing Key Laboratory of Materials Utilization of Nonmetallic Minerals and Solid Wastes, National Laboratory of Mineral Materials, School of Materials Science and Technology, China University of Geosciences, Beijing 100083, China.

+ Department of Environmental Engineering, Zhejiang University, Hangzhou 310027, China.

§ Department of Civil and Environmental Engineering, The Hong Kong Polytechnic University, Hong Kong, China.

* To whom correspondence should be addressed. E-mail: dfctbu@126.com (Fan Dong). Phone: +86 23 62769785 605. Fax: +86 23 62769785 605.

Abstract: Earth-abundant insulators are seldom exploited as photocatalysts. In this work, we constructed a novel family of insulator-based heterojunctions and demonstrated their promising applications in photocatalytic NO purification, even under visible light irradiation. The heterojunction formed between the insulator $SrCO_3$ and the photosensitizer BiOI, via a special $SrCO_3$-BiOI core-shell structure, exhibits an enhanced visible light absorbance between 400–600 nm, and an unprecedentedly high photocatalytic NO removal performance. Further density functional theory (DFT) calculations and X-ray photoelectron spectroscopy (XPS) analysis revealed that the covalent interaction between the O 2p orbital of the insulator ($SrCO_3$, n-type) and the Bi 6p orbital of photosensitizer (BiOI, p-type) can provide an electron transfer channel between $SrCO_3$ and BiOI, allowing the transfer of the photoexcited electrons from the photosensitizer to the conduction band of insulator (confirmed by charge difference distribution analysis and time-resolved fluorescence spectroscopy). The $\bullet O_2^-$ and •OH radicals are the main reactive species in photocatalytic NO oxidation. A reaction pathway study based on both *in situ* FT-IR and molecular-level simulation of NO adsorption and transformation indicates that this heterojunction can efficiently transform NO to harmless nitrate products via the $NO \rightarrow NO^+$ and $NO_2^+ \rightarrow$nitrate or nitrite routes. This work provides numerous opportunities to explore earth-abundant insulators as visible-light-driven photocatalysts, and also offers a new mechanistic understanding of the role of gas-phase photocatalysis in controlling air pollution.

1. Introduction

Air pollution is one of the major challenges faced by developing countries. The NO_x emitted from fossil fuel combustion and automobile exhausts is one of the main contributors to acid rain and photochemical smog, and endangers human health and the environment.[1] Although some traditional technologies (SCR, absorption, adsorption) are available for the treatment of high concentration NO_x emissions, they are not economically feasible for the purification of the low concentration NO_x in the atmosphere.[2, 3] Photocatalysis is an alternative technology and has great potential for removal of NO_x at ppb level, as it is environmentally friendly with little secondary pollution and can be driven directly by sunlight irradiation.[4] Therefore, numerous efforts have been made to develop efficient photocatalysts to achieve the high performance necessary for environmental applications.[5,6] Currently, semiconductors (TiO_2,[7] Bi-based compounds,[8] g-C_3N_4[9,10]) and some plasmonic metals (Au, Ag and Bi) have been used as photocatalysts for NO_x abatement.[11-13] Modification strategies, such as doping,[14] coupling,[15] photosensitization[16] and deposition[17], can improve the photocatalytic performance. For the environmental application of photocatalysts, the requirements of low-cost, abundance and high performance should be fulfilled.

Earth-abundant insulators are widely used in the electronics, ceramics, and glass industries, but are rarely used as photocatalysts because their band gap is typically larger than those of semiconductors.[18] Similar to the semiconductor, the insulator has separate valence and conduction bands, which can be modified to allow them to function as new photocatalyst. Recently, Dong et al. discovered a defective insulator and demonstrated decent photocatalytic activity under ultraviolet light irradiation owing to the defect-mediated formation of midgap states in the band structure.[19]

Visible light accounts for 50% of the solar spectrum, far exceeding the proportion of ultraviolet

light (4%). If the light absorption spectra of insulators are extended into the visible light range, great potential can be envisioned for the application of insulator-based photocatalyst in environmental remediation.

Various strategies have been developed to modify photocatalysts with a wide band gap, among which, photosensitization has shown promising results in promoting efficient visible light photocatalysis.[20,21] The light absorption spectra of semiconductors with wide band gap can be extended into the visible region by the use of a photosensitizer that matches the band structure of the semiconductor.[22,23] Specific dyes, such as narrow band-gap semiconductors (BiOI and AgI) and graphene oxide (GO) can be acted as photosensitizers.[23-25] The conduction band of insulators, which are similar to those of semiconductors, could potentially accept photoexcited electrons from the photosensitizer. Thus, we propose broadening the light absorption spectra of the insulator into the visible light range by coupling with a photosensitizer, on the basis that the energy band level can be properly designed. This concept could harness the photosensitization effect to allow insulators to achieve visible light photocatalysis. To the best of our knowledge, an insulator-based nanocomposite with visible-light-driven photocatalytic performance has never been reported, and the underlying mechanisms need to be unraveled.

In this work, we constructed an insulator-based nanocomposite (core-shell structured $SrCO_3$-BiOI heterojunction) with high photocatalytic NO removal performance under visible light irradiation, despite the negligible photocatalytic activity of $SrCO_3$ or BiOI alone. Based on a highly combined experimental and theoretical investigation, we found that the covalent interaction between the O 2p orbital of the insulator ($SrCO_3$, n-type) and the Bi 6p orbital of the photosensitizer (BiOI, p-type) induced the formation of an electron transfer channel between $SrCO_3$ and BiOI. This special channel

facilitated the transfer of photoexcited electrons from the photosensitizer to the conduction band of the insulator by the formation of a p-n junction. In situ Fourier-transform infrared spectroscopy (FT-IR) was employed to monitor the reaction intermediates and products dynamically. It is important to investigate whether this insulator-based nanocomposite could efficiently transform NO and potentially toxic intermediates to harmless products via visible light photocatalysis. This new concept can be extended to develop a family of insulator-based heterojunctions via the combination of different insulators and photosensitizers, such as the coupling of $BaCO_3$ with BiOI or $SrCO_3$ with AgI (Figure S1 and S2). Thus, the present work opens numerous opportunities to explore other earth-abundant insulators as visible-light-driven photocatalysts to control air pollution.

2. Experimental and theoretical section

2.1 Preparation of $SrCO_3$-BiOI core-shell heterojunction

All chemicals were of analytical grade and were used without further treatment. The catalysts were prepared by a facile precipitation method. In a typical preparation, $Bi(NO_3)_3•5H_2O$ (Sigma-Aldrich) was dissolved in 100 mL glycol solution (90 mL deionized water and 10 mL glycol), following which 3.0 mmol of $SrCO_3$ (Sigma-Aldrich) was added to the above solution and stirred for 30 min. A KI solution (30 mL) was added dropwise and stirred for 2 h (the molar ratio of $Bi(NO_3)_3•5H_2O$ and KI were controlled at 1:1). The resultant precipitates were washed twice with deionized water and ethanol and dried at 60 °C for 12 h to obtain the final product. The molar ratio of $SrCO_3$ and BiOI was controlled at 6:3, 6:4, and 6:5 and samples were correspondingly labeled as Sr-B-X (X = 3, 4, 5). For comparison, pristine BiOI was prepared via the same process without the addition of $SrCO_3$.

2.2 Characterization methods

The crystal structure of the samples was recorded using a powder X-ray diffractometer with Cu

Kα radiation (Model D/Max RA, Rigaku Co, Japan). X-ray photoelectron spectroscopy with an Al Kα X-ray radiation source (Thermo ESCALAB 250, USA) was used to analyze the chemical composition of the samples. A UV-vis diffuse spectrophotometer was used to analyze the optical properties of the samples with 100% $BaSO_4$ as a reference (UV2550, Shimadzu, Japan). The photoelectrochemical and Mott−Schottky measurements were recorded by an electrochemical system with a three-electrode quartz cell and 0.1 M Na_2SO_4 as the electrolyte (CHI-660B, China). The morphological structure was measured by scanning electron microscopy (SEM) and transmission electron microscopy (TEM) (SEM: JEOL Model JSM-6490, Japan; TEM: JEM-2010, Japan). The Brunauer–Emmett–Teller (BET) specific surface area and pore structure measurements were carried out using an ASAP 2020 apparatus. Time-resolved fluorescence decay spectra were collected using a fluorescence spectrophotometer (Edinburgh Instruments, FLSP-920). Electron spin resonance (ESR) spectra of radicals that were spin-trapped using 5, 5-dimethyl-1-pyrroline N-oxide (DMPO) were recorded using a JES FA200 spectrometer.

2.3 Application of insulator-based heterojunction in photocatalytic NOx purification

The photocatalytic performance was evaluated by removing NO (present at ppb levels) from a continuous stream reactor (Figure S3). A UV cut-off filter (420 nm) was applied to remove UV light for the test of photocatalytic activity in visible light region (420–700 nm). The average light intensity on the catalyst is 0.16 $W \cdot cm^{-2}$. For this, 0.2 g of the sample was ultrasonically dispersed on two 12-mm diameter glass disks and dried at 60 °C. After natural cooling, the glass disks were placed in the continuous stream reactor. When the NO concentration reached the adsorption-desorption equilibrium, the lamp was turned on. A NO_x analyzer (Thermo Scientific, 42i-TL, USA) recorded the concentrations of NO, NO_2, and NO_x ($NO + NO_2$) every minute. The removal ratio (η) of NO was

calculated using η (%) = (1–C/C_0) × 100 %, where C represents the NO concentration at the outlet of the reactor after turning on the lamp, and C_0 represents the NO concentration when the adsorption-desorption equilibrium is reached before turning on.

2.4 Density functional theory calculations

DFT calculations were introduced using the "Vienna *ab initio* simulation package" (VASP5.4) and a generalized gradient correlation function.[26-28] A plane-wave basis set with a cut-off energy at 400 eV and the projector-augmented wave method framework was adopted. The Gaussian smearing width was placed at 0.2 eV.[29, 30] The Brillouin zone was sampled with a 3 × 3 × 1 Monkhorst Pack grid. All atoms were allowed to converge to 0.01 eV $Å^{-1}$. The 8 × 8 × 8 supercell of BiOI included 8 oxygen atoms, 8 bismuth atoms, and 8 iodine atoms, and the 10 × 15 × 17 supercell of $SrCO_3$ included 52 oxygen atoms, 16 strontium atoms, and 16 carbon atoms. The supercells were first relaxed, before the BiOI supercell was placed on the plane of $SrCO_3$.[31,32]

2.5 *In situ* FT-IR investigation of the photocatalytic NO oxidation mechanism

In situ FT-IR measurements were recorded using a Tensor II FT-IR spectrometer (Bruker), *in situ* reaction bin, gas system, light source, and pretreatment equipment (Figure S4). The real-time FT-IR spectrum was used as a background after a heat treatment (110 °C) under high-purity He. Then, the reaction gas (50 mL/ min NO and 50 mL/ min O_2) was sent to the reaction chamber. Because of the detection limit of *in situ* FT-IR measurement, the concentration in the activity test (ppb level) is too low to be detected. Therefore, NO with 50 ppm is introduced into the reactor. Under dark conditions, the samples were subjected to 20-min adsorption reactions. Afterwards, the photocatalytic reaction process was carried out for 60 min under visible light irradiation. Finally, the lamp was turned off. The IR spectra were recorded at a given time interval. The scanned area of the infrared spectrum was

158 4000–600 cm^{-1}.

159 The normalized curve is prepared in the following way. In the adsorption process, the value of the
160 baseline is taken as 0, and the maximum value of the adsorption process is normalized as 1, and the
161 other values are calculated as relative values to the maximum value. During the reaction, the value of
162 adsorption equilibrium is taken as 0, and the maximum value of the reaction process is normalized as
163 1, the other values are calculated as relative values to the maximum value.

164 ## 3. Results and Discussion

165 ### 3.1 Microstructure and optical properties.

166 XRD analysis was conducted to identify the crystal phase of the insulator-based $SrCO_3$-BiOI
167 heterojunction (Sr-B-X, X=3, 4, 5), and the results are shown in Figure 1a. The typical diffraction
168 peaks of tetragonal BiOI (JCPDS 10-0445) and orthorhombic $SrCO_3$ (JCPDS 05-0418) are both
169 observed in Sr-B-X (X=3, 4, 5). The survey XPS spectra show all samples contained Bi, O, I, Sr and
170 C elements (Figure 1b). These results indicate that the $SrCO_3$-BiOI composites have been
171 successfully prepared.

172 UV-vis diffuse reflectance spectra (Figure 1c) shows that $SrCO_3$ as a typical insulator has a large
173 band gap of 4.43 eV (absorption edge at 280 nm), while the BiOI semiconductor has a narrow band
174 gap of 1.88 eV and exhibits little photocurrent response (Figure 1d). After the formation of
175 $SrCO_3$-BiOI heterojunction, the light absorbance spectra of the Sr-B-X (X=3, 4, 5) can be extended
176 to a width of 600 nm. This extension can be ascribed to the interplay between the photosensitizer
177 (BiOI) and the insulator ($SrCO_3$), resulting in the enhanced light-harvesting ability of Sr-B-X.[33]
178 Figure 1d shows that $SrCO_3$ or BiOI alone exhibit little photocurrent response under visible light
179 irradiation, which can be attributed to the large band gap of $SrCO_3$ and the fast recombination of

photogenerated electrons and holes in BiOI.[34] After the formation of the insulator-based $SrCO_3$-BiOI heterojunction, the photocurrent Sr-B-4 photocurrent was dramatically enhanced. This finding shows that the photoexcited e^- - h^+ pairs could be effectively separated in the insulator-based heterojunction.[23]

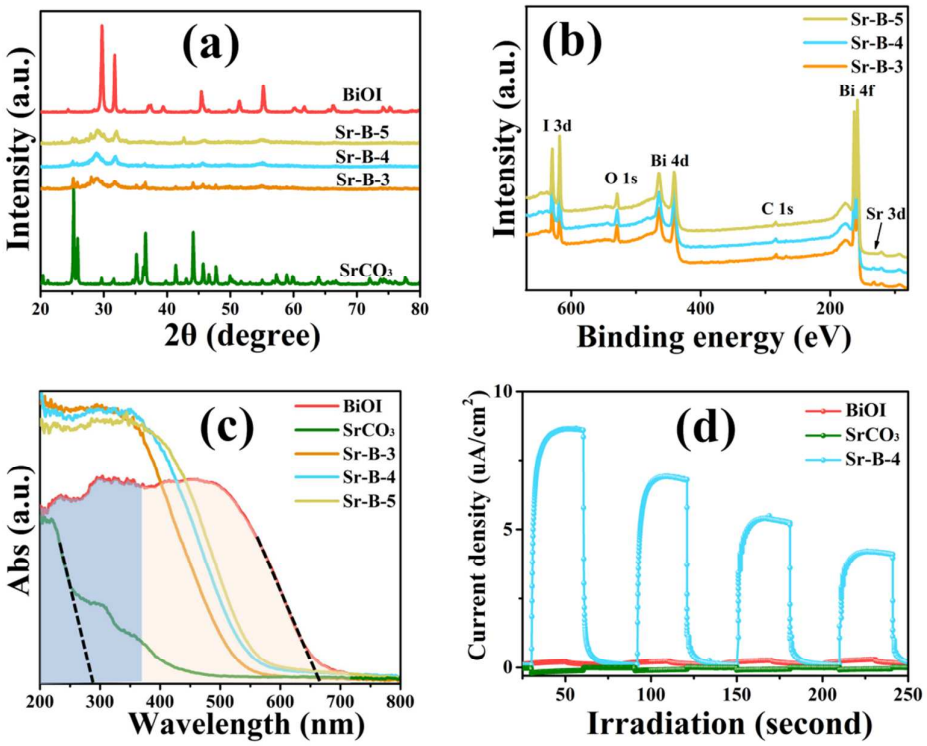

Figure 1. XRD patterns (a), XPS-survey spectra (b), UV-vis diffuse reflectance spectra (c) and photocurrent density (d).

SEM and TEM images of pure BiOI and $SrCO_3$ are shown in Figure S5. BiOI is constructed of nanosheets and $SrCO_3$ is comprised of nanorods. Energy-dispersive X-ray (EDX) elemental mapping (Figure 2a) and TEM images of Sr-B-4 (Figure 2b-2c) clearly revealed that BiOI is evenly distributed on the surface of $SrCO_3$ nanorods, forming an open $SrCO_3$-BiOI core-shell structure. Figure 2d shows lattice spacings of 0.282 and 0.365 nm, which correspond to the (110) plane of BiOI and (111) plane of $SrCO_3$, respectively. A border between $SrCO_3$ and BiOI can be observed, which

implies that an intimate interface is formed. This interface is favorable for the transfer of charge carriers between $SrCO_3$ and BiOI, which could also account for the significantly improved charge separation and photocurrent density in the Sr-B-4.[35] Figure S6 and Table S1 show that the Sr-B-X catalysts possess a mesoporous structure with large specific surface areas, which is beneficial for the adsorption of contaminants and diffusion of final products.[35]

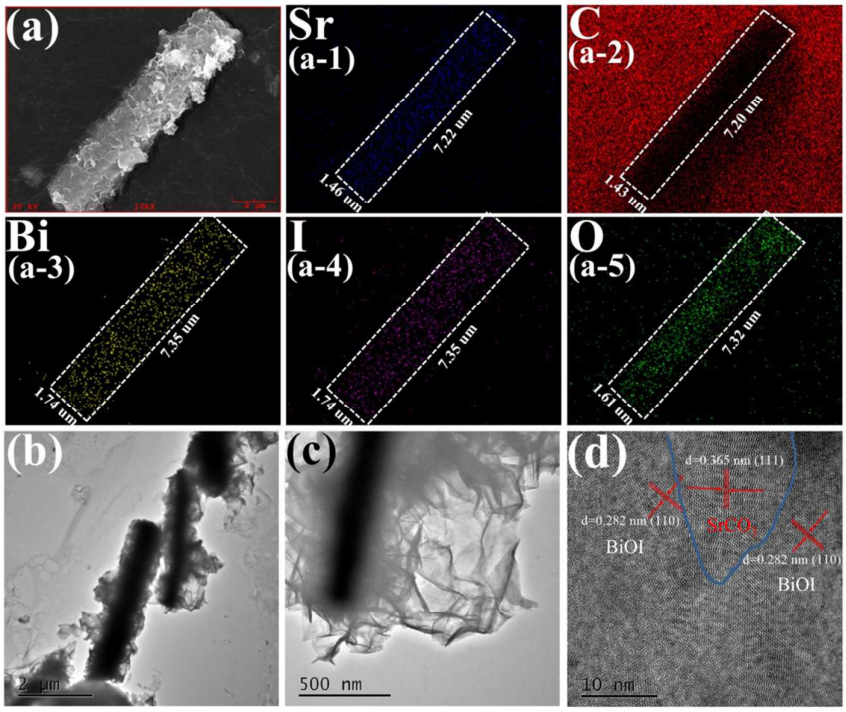

Figure 2. SEM image of Sr-B-4 (a) EDX elemental mapping of Sr (a-1), C (a-2), Bi (a-3), I (a-4) and O (a-5) in (a), TEM images (b, c) and HRTEM image of Sr-B-4 (d).

3.2 Charge separation and transfer.

Density functional theory (DFT) was extensively employed in calculations of the electronic structure to confirm the nature of the interaction between insulator ($SrCO_3$) and the photosensitizer (BiOI) in the insulator-based $SrCO_3$-BiOI core-shell heterojunction. The electron localization function (ELF) shows a strong covalent interaction between Bi atoms of BiOI and O atoms of $SrCO_3$ (Figure 3a). The projected density of states (PDOS) was also calculated (Figure 3b). The peaks

(named as α, β, γ, and δ) of the Bi 6p and O 2p orbitals in BiOI and $SrCO_3$, respectively, were overlapped. This overlap suggests that an electron transfer channel is constructed by the covalent interaction between the Bi 6p and O 2p orbitals within the $SrCO_3$-BiOI core-shell heterojunction. This unique electronic interaction enables electron transfer between the insulator ($SrCO_3$) and photosensitizer (BiOI). The charge difference distribution is calculated to determine the electron transfer direction between them, as shown in Figure 3c. The Bi atoms of BiOI, which is charge depleted, are shown in green, and the O atoms of $SrCO_3$, where charge accumulates, are shown in purple. This result predicts that the electron transfer direction and pathway is from Bi 6p orbital of BiOI to the O 2p orbital of $SrCO_3$.

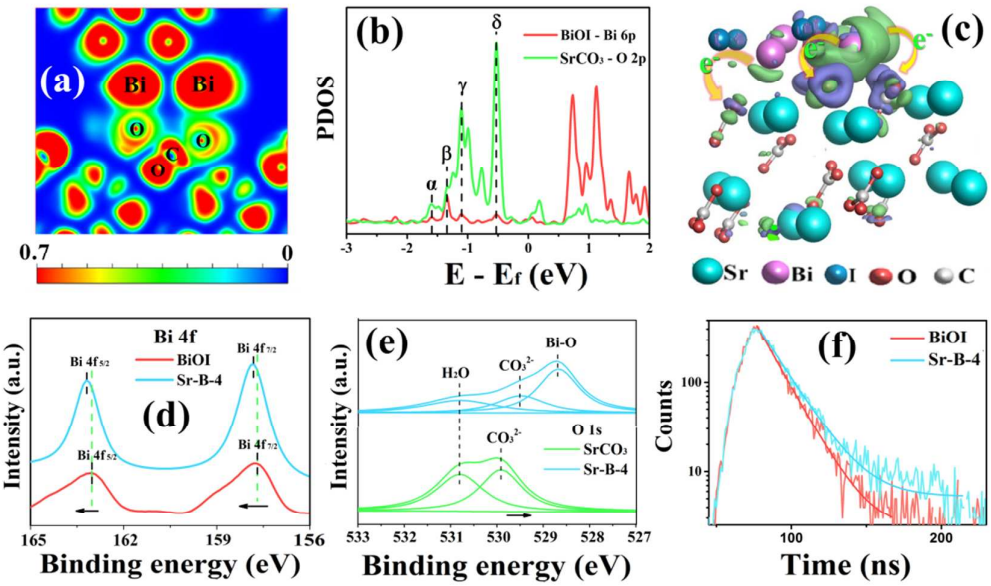

Figure 3. (a) Electron location function (ELF); (b) projected density of states (PDOS) of Bi atoms in BiOI and O atoms in $SrCO_3$: the Fermi level is set to 0 eV; (c) Charge difference distribution between BiOI and $SrCO_3$: charge accumulation is in purple and depletion in green, and the isosurface is set to 0.003 eV $Å^{-3}$; (d) XPS spectra of Bi 4f, (e) O 1s, and (f) nanosecond-level time-resolved fluorescence spectra surveyed at room temperature.

XPS results show that the binding energies for Bi 4f (Figure 3c) and I 3d (Figure S7a) in the Sr-B-4 shifted to higher values compared to those in pure BiOI, whereas the binding energies for O 1s (Figure 3d) and C 1s (Figure S7b) in Sr-B-4 were shifted to a lower value in comparison with pure $SrCO_3$. These chemical shifts experimentally demonstrate that the electrons transfer from Bi and I atoms of BiOI to O and C atoms of $SrCO_3$ in the $SrCO_3$-BiOI core-shell heterojunction (Sr-B-4), consistent with theoretical calculation (Figure 3c).[36] Furthermore, nanosecond-level time-resolved fluorescence decay spectroscopy is used to study the photo-induced charge-transfer dynamics on BiOI and Sr-B-4 (Figure 3f). The radiative lifetime is prolonged from 0.69 ns for BiOI to 0.80 ns for Sr-B-4. This lifetime extension is attributed to the transfer pathway from the BiOI shell to the $SrCO_3$ core in Sr-B-4, leading to increased charge separation and transfer in $SrCO_3$-BiOI heterojunction. The DFT and experimental results both confirm that the Bi 6p orbital of BiOI covalently interacts with the O 2p orbital of $SrCO_3$ to form an electron transfer channel, enabling photo-induced electrons in BiOI to be transferred to the conduction band of the insulator ($SrCO_3$) in the $SrCO_3$-BiOI core-shell heterojunction.

3.3 Active species and visible light photocatalytic performance.

The photo-generated radical species are investigated by DMPO ESR spin-trapping. Figure 4a and 4b show that pure $SrCO_3$ has no ESR signal under visible light irradiation because the band gap is so large that $SrCO_3$ alone cannot be excited sufficiently to produce charge carriers. In contrast, the $SrCO_3$-BiOI heterojunction could produce a significant of both $\bullet O_2^-$ and •OH radicals, which are typically reactive species for subsequent reactions. As demonstrated previously, the photo-induced electrons in BiOI could be transferred to the conduction band of $SrCO_3$. These electrons on $SrCO_3$ could reduce the O_2 to form $\bullet O_2^-$ radicals. The •OH radicals are generated via the oxidization of the

OH^- ($OH^- + h^+ \rightarrow \bullet OH$) by the holes left in the valence band of BiOI.[37] The $SrCO_3$-BiOI heterojunction is applied in photocatalytic air purification taking NO as target pollutant. The NO removal ratio of Sr-B-4 dramatically is increased to 48.3% under visible light irradiation in comparison with the physical mixture of $SrCO_3$ and BiOI (Sr-B-M, 24.7%), pure BiOI with low activity (6.0%) and pure $SrCO_3$ with no activity (0.0%). The low activity of BiOI arises from the rapid charge recombination rate and weak redox ability. To the best of our knowledge, this is the most efficient performance yet reported for an insulator-based photocatalyst, and is even better than the performance of some well-known semiconductor-based photocatalysts, such as BiOBr (21.3%),[38] C-doped TiO_2 (21.8%),[39] I-intercalated $BiOIO_3$ (44.1%),[40] and $(BiO)_2CO_3$ (43.5%).[41] In addition, the photocatalytic performance is stable without deactivation after testing for five consecutive cycles (Figure 4d). The present new concept has already been applied in the development of a family of insulator-based heterojunction via the combination of different insulators and photosensitizers, such as the coupling of $BaCO_3$ with BiOI or $SrCO_3$ with AgI. The $BaCO_3$-BiOI and $SrCO_3$- AgI heterojunctions demonstrate highly enhanced photocatalytic NO purification performance under visible light irradiation (Figure S1 and S2).

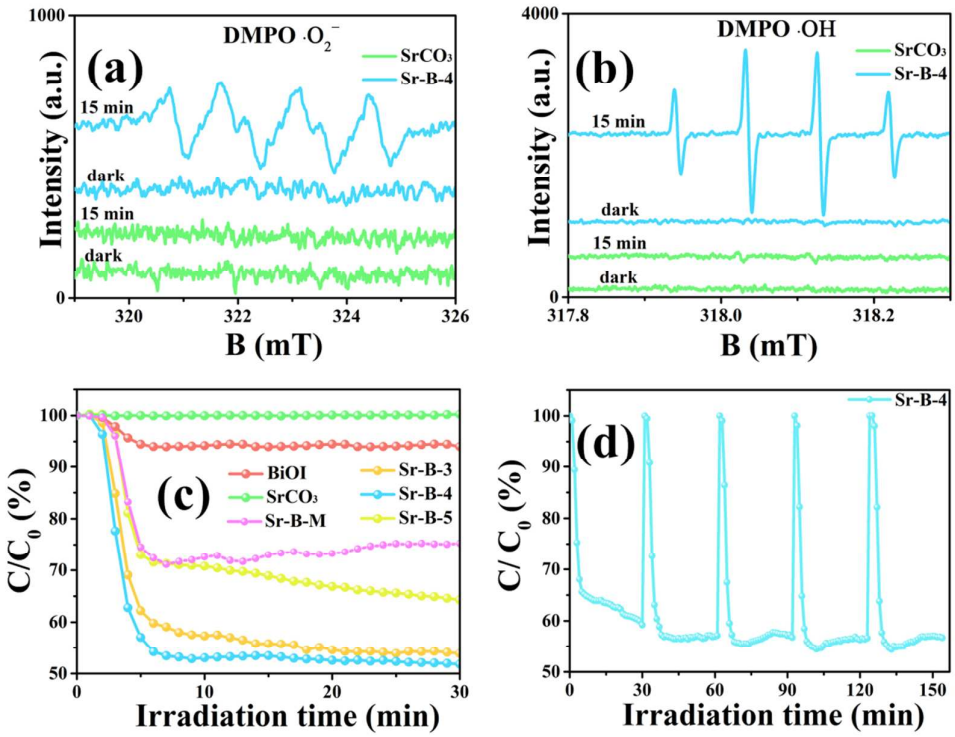

Figure 4. DMPO ESR spin-trapping of Sr-B-4 and $SrCO_3$ for $\bullet O_2^-$ (a) and •OH (b) radicals. Photocatalytic NO purification curves of all the samples (c) and stability tests for Sr-B-4 (d) under visible light illumination.

3.4 *In situ* FT-IR investigation of the NO adsorption and transformation pathway.

In situ FT-IR is carried out to investigate the pathway of photocatalytic NO purification for the insulator-based $SrCO_3$-BiOI heterojunction and to monitor the evolution of the reaction intermediates and final products on the photocatalyst surface. Under dark conditions, a number of adsorption peaks appear after NO and O_2 are introduced onto the photocatalyst surface (Figure 5a). The chemical adsorption and polymerization of NO cause characteristic N_2O_3 (960 cm^{-1}), N_2O_2 (1628 cm^{-1}), NO_2^+ (1947 and 2084 cm^{-1}), and NO_2 (3503 and 3582 cm^{-1}) peaks to appear, and undissociated H_2O (3375 cm^{-1}) can also be observed (Equation 1-3).[42-43] The detected nitrite (NO_2^-, 1084 and 1179 cm^{-1}) peaks are attributed to the disproportionation of N_2O_4 in the presence of water

(Equation 5).[44,45] The normalized absorbance curve clearly shows that the amounts of the adsorbed NO_2 and nitrites accumulated on the photocatalyst surface increased with time (Figure 5c). The adsorption-desorption equilibrium is achieved in 20 min. An adsorption mechanism is proposed, as shown in Equation (1-5).

$$2NO \leftrightarrows N_2O_2 \quad (1)$$

$$2NO + O_2 \rightarrow 2NO_2 \quad (2)$$

$$NO + NO_2 \rightarrow N_2O_3 \quad (3)$$

$$2NO_2 \leftrightarrows N_2O_4 \quad (4)$$

$$N_2O_4 + H_2O \rightarrow NO_2^+ + OH^- + HNO_2 \quad (5)$$

After the adsorption period, the visible light source is turned on, and the photocatalytic reaction is initiated. The whole photocatalytic NO purification process is recorded dynamically as shown in Figure 5b. The spectrum of "ad-eq" is same as that of "20 min" in the adsorption process. Under visible light irradiation, new absorption bands at 1003, 1113, and 1552 cm^{-1} appear, indicating the production of nitrate (NO_3^-) ions on the catalyst surface via photocatalytic NO oxidation by the reactive radicals. The peak intensity at 1179 and 1084 cm^{-1} is obviously increased, which can be attributed to the generation of nitrites. It is worth noting that the absorption bands of some adsorption products of N_2O_2 (1628 cm^{-1}), NO_2 (3503, 3582 cm^{-1}), and undissociated H_2O (3375 cm^{-1}) are consumed and disappear during the visible light irradiation but appear again after turning off the light. The peak of N_2O_3 (948 cm^{-1}) also increased during the photocatalytic reaction, yet the intensity of the peak remained relatively weak, indicating that N_2O_3 is consumed as it is generated (Equation 3, 6-7, 10-11). The absorption bands of NO^+ (1690 and 2223 cm^{-1}) and NO_2^+ (1980 and 2144 cm^{-1}) can also be observed (Figure S9). These reaction intermediates are generated by the oxidation of NO and

289 NO_2 by •OH and $•O_2^-$ and are finally oxidized to nitrites or nitrates. The results suggest that the
290 insulator-based $SrCO_3$-BiOI core-shell heterojunction could transform NO, NO-related adsorption
291 products, and intermediates into the final products of nitrites and nitrates via visible light
292 photocatalysis. These final products accumulated on the photocatalyst surface can be easily removed
293 by water washing and the photocatalyst can be regenerated via this facile method.[46-47]

294 NO_2 and N_2O_4 are more toxic than NO as an air pollutant, and thus the conversion of NO into NO_2
295 should be largely inhibited. In some cases, the NO_2 may be released into the air, leading to secondary
296 pollution if the photocatalysis efficiency is not high enough. In this work, NO_2 is produced and
297 accumulates on the catalyst surface during the adsorption stage (Figure 5c). The normalization
298 absorbance curves in Figure 5d show that all the NO_2 can be transformed into a stable final product
299 of nitrates/nitrites by the abundant reactive photo-generated radicals ($NO_2 \rightarrow NO_2^+ \rightarrow$nitrate). The
300 absorption band of H_2O decreased as the photocatalytic reaction progressed as H_2O is consumed in
301 the formation of •OH radicals and transformation of NO_x.[40] Both the $•O_2^-$ and •OH radicals are
302 involved in the photocatalytic oxidation reactions (Figure 4a and 4b).[22] Based on these results, the
303 reaction mechanism of photocatalytic NO oxidization by an insulator-based heterojunction is
304 proposed as shown in Equation (6-18). The present work demonstrates the first earth-abundant
305 insulator-based heterojunction photocatalysts that can efficiently transform NO and potentially toxic
306 intermediates to harmless final products via visible light photocatalysis.

Reaction pathway 1: $NO \rightarrow N_2O_3 \rightarrow NO_2 \rightarrow NO_2^+ \rightarrow NO_3^-$

$$2NO + 2\cdot OH \rightarrow N_2O_3 + H_2O \quad (6)$$

$$N_2O_3 + 2\cdot OH \rightarrow 2NO_2 + H_2O \quad (7)$$

$$NO_2 + \cdot OH \rightarrow NO_2^+ + OH^- \quad (8)$$

$$NO_2^+ + 2OH^- \rightarrow NO_3^- + H_2O \quad (9)$$

$$6NO + 2{\cdot}O_2^- + H_2O \rightarrow 3N_2O_3 + 2OH^- \quad (10)$$

$$3N_2O_3 + 2{\cdot}O_2^- + H_2O \rightarrow 6NO_2 + 2OH^- \quad (11)$$

$$NO_2 + {\cdot}O_2^- + 2e^- + 2H_2O \rightarrow NO_2^+ + 4OH^- \quad (12)$$

$$NO_2^+ + H_2O \rightarrow NO_3^- + 2H^+ \quad (13)$$

Reaction pathway 2: NO → NO^+ → NO_3^- (NO_2^-)

$$NO + {\cdot}OH \rightarrow NO^+ + OH^- \quad (14)$$

$$NO^+ + 2{\cdot}OH + 2\,OH^- \rightarrow NO_3^- + 2H_2O \quad (15)$$

$$NO + {\cdot}O_2^- + 2e^- + 2H_2O \rightarrow NO^+ + 4OH^- \quad (16)$$

$$NO^+ + {\cdot}O_2^- + e^- \rightarrow NO_3^- \quad (17)$$

$$NO^+ + OH^- + e^- \rightarrow NO_2^- + H_2O \quad (18)$$

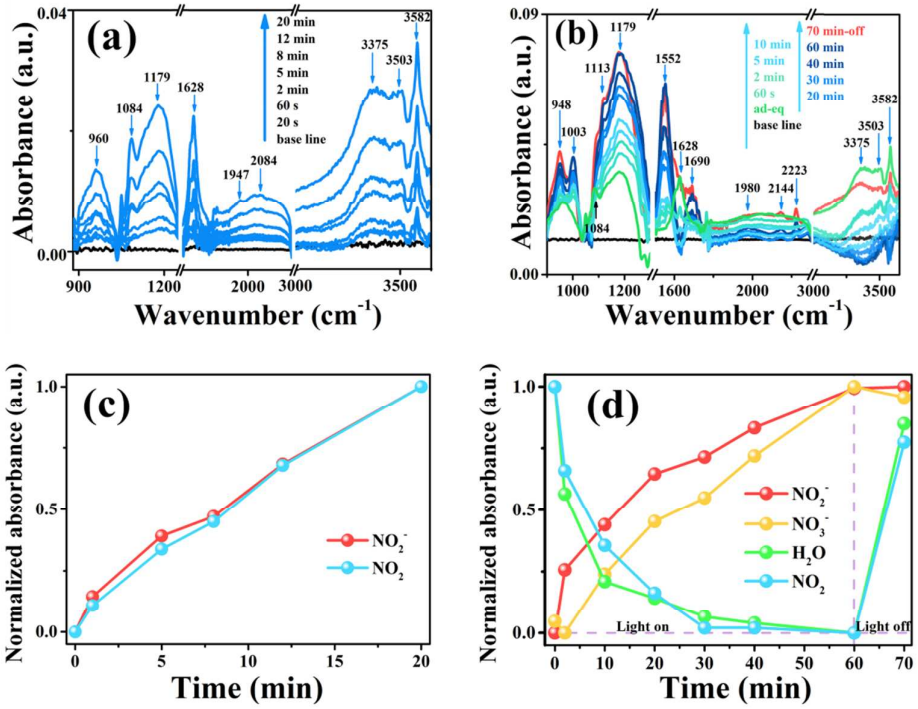

Figure 5. *In situ* FT-IR spectra of the NO adsorption process (a) and corresponding normalized absorbance curves (c). Photocatalytic NO oxidation process: the adsorption curve is in yellow and the FT-IR curve after switching the light off for 10 min is in red (b) and corresponding normalized

absorbance curves (d) over Sr-B-4 under visible light irradiation.

3.5 Mechanisms of Photocatalysis on insulator-based $SrCO_3$-BiOI heterojunction.

In this work, we employ a simple precipitation method to construct an insulator-based $SrCO_3$-BiOI core-shell heterojunction, which is capable of highly efficient visible-light-driven photocatalytic NO conversion. The conversion pathway of photocatalytic NO oxidation is revealed by time-dependent in situ FT-IR (Figure 6a). Combined with the results of DFT calculation and experimental characterizations, the proposed photocatalytic mechanism is illustrated in Figure 6b.

The valence band (VB) and conduction band (CB) of $SrCO_3$ and BiOI are determined by equation 21 and 22.[48]

$$E_{VB} = X - E^e + 0.5\ E_g \qquad (21)$$

$$E_{CB} = E_{VB} - E_g \qquad (22)$$

Where E_g represents the band gap of the semiconductor. X is the electronegativity of the semiconductor, which is calculated from the electronegativity of the constituent atoms. The X values of $SrCO_3$ and BiOI are calculated to be 5.57 and 6.21 eV, respectively. E^e is the energy of free electrons on the hydrogen scale (~4.5 eV). The band gaps of $SrCO_3$ and BiOI are calculated to be 4.43 and 1.88 eV, respectively. For $SrCO_3$, the E_{VB} and E_{CB} are estimated to be 3.28 and −1.15 eV, respectively. The E_{VB} and E_{CB} of BiOI are estimated to be 2.65 and 0.74 eV, respectively. It appears that the band structures of $SrCO_3$ and BiOI do not match sufficiently to form an effective heterojunction. However, the Mott-Schottky plot confirms $SrCO_3$ to be an n-type material where the Fermi level is located close to the conduction band (CB) (Figure S8). BiOI is a typical p-type semiconductor with a Fermi level close to the valence band (VB).[22] The coupling of a p-type photosensitizer (BiOI) to an n-type insulator ($SrCO_3$) enables the Fermi level of BiOI and $SrCO_3$ to

shift to the same level and to reach equilibrium, forming a p-n heterojunction. Eventually, the CB of $SrCO_3$ is shifted to an energy level lower than that of BiOI. Once the insulator-based heterojunction is exposed to visible light, the photoexcited electrons of the photosensitizer BiOI can migrate to the CB of insulator ($SrCO_3$) under the driving force of the energy difference between the CB of BiOI and $SrCO_3$. This finding also favors the electron-hole pairs' separation on BiOI. The electrons on the CB of $SrCO_3$ could react with the O_2 to produce the $\bullet O_2^-$ radicals. The residual holes in the VB of BiOI in the heterojunction react with the OH^- to produce •OH radicals. These two radicals are primarily responsible for the remarkable visible light photocatalytic NO removal on the insulator-based $SrCO_3$-BiOI core-shell heterojunction.

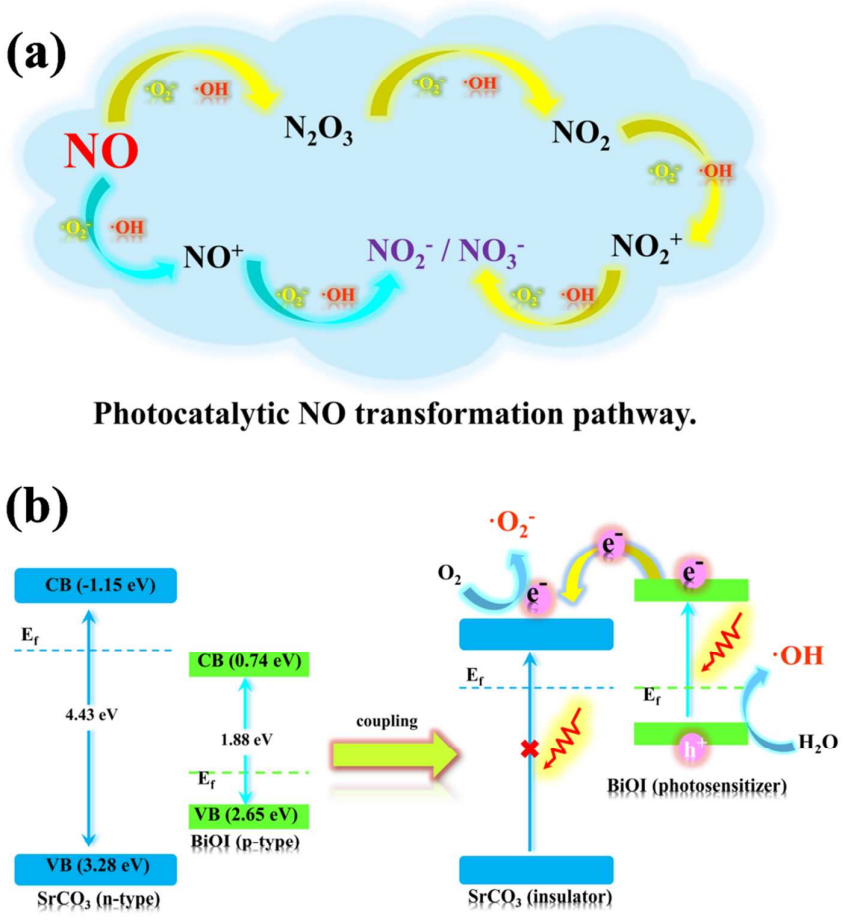

Photocatalytic NO transformation pathway.

Figure 6. Photocatalytic NO transformation pathway (a) and visible light photocatalysis mechanism

of the insulator-based $SrCO_3$-BiOI core-shell heterojunction (b).

Associated Content

Supporting Information

Photocatalytic NO purification curves of $BaCO_3$, BiOI, and $BaCO_3$-BiOI heterojunction (Figure S1). Photocatalytic NO purification curves of $SrCO_3$ and $SrCO_3$-AgI heterojunction (Figure S2). Thermo NO_x analyzer (a), Continuous stream reactor (b), Visible light source (c) and photocatalytic NO_x reaction system under working condition (d) (Figure S3). *In situ* reaction bin and loading parts (a), Pretreatment equipment and light source (b), Tensor II FT-IR spectrometer (c) and *in situ* FT-IR measurement under working conditions (d) (Figure S4). SEM (a) and TEM (b) of pure BiOI; SEM (c) and TEM (d) of pure $SrCO_3$ (Figure S5). N_2 adsorption-desorption isotherms (a) and the corresponding pore-size distribution curves (b) (Figure S6). XPS spectra of the I 3d (a) and C 1s (b) (Figure S7). Mott-Schottky curves of $SrCO_3$ (Figure S8). *In situ* FT-IR spectra of photocatalytic NO oxidation process in the range of 1870–2300 cm^{-1} (Figure S9). S_{BET}, total pore volume, pore size and NO removal ratio for $SrCO_3$, BiOI, Sr-B-3, Sr-B-4 and Sr-B-5 (Table S1). Assignments of the IR bands observed during adsorption and photocatalytic NO oxidation processes over Sr-B-4 (Table S2).

ACKNOWLEDGMENTS

This work was supported by the National Natural Science Foundation of China (21777011, 21501016 and 51478070), the National Key R&D Plan (2016YFC02047), the Innovative Research Team of Chongqing (CXTDG201602014), the Key Natural Science Foundation of Chongqing (cstc2017jcyjBX0052). The authors also acknowledge the AM-HPC in Suzhou, China for computational support.

Author Contributions

The manuscript was written through contributions of all authors. All authors have given approval to the final version of the manuscript.

References

1. Lewis, A.; Edwards, P. Validate personal air-pollution sensors: Alastair Lewis and Peter Edwards call on researchers to test the accuracy of low-cost monitoring devices before regulators are flooded with questionable air-quality data. *Nature.* **2016,** *535* (7610), 29-32.
2. Misra, C.; Ruehl, C.; Collins, J.; Chernich, D.; Herner, J. In-Use NOx Emissions from Diesel and Liquefied Natural Gas Refuse Trucks Equipped with SCR and TWC, Respectively. *Environ. Sci. Technol.* **2017,** *51* (12), 6981-6989.
3. Seneque, M.; Can, F.; Duprez, D.; Courtois, X. NOx Selective Catalytic Reduction (NOx-SCR) by Urea: Evidence of the Reactivity of HNCO, Including a Specific Reaction Pathway for NOx Reduction Involving NO + NO_2. *ACS. Catal.* **2016,** *6* (7), 4064-4067.
4. He, Y.; Zhang, L.; Teng, B.; Fan, M. New application of Z-scheme Ag_3PO_4/g-C_3N_4 composite in converting CO_2 to fuel. *Environ. Sci. Technol.* **2015,** *49* (1), 649-656.
5. Wang, Y.; Wang, Q.; Zhan, X.; Wang, F.; Safdar, M.; He, J. Visible light driven type ii heterostructures and their enhanced photocatalysis properties: A review. *Nanoscale.* **2013,** *5* (18), 8326-8339.
6. Moniz, S. J. A.; Shevlin, S. A.; Martin, D. J.; Guo, Z. X.; Tang, J. Visible-light driven heterojunction photocatalysts for water splitting–A critical review. *Energ. Environ. Sci.* **2015,** *8* (3), 731-759.
7. Sajan, C. P.; Wageh, S.; Al-Ghamdi, A. A.; Yu, J.; Cao, S. TiO_2 nanosheets with exposed {001} facets for photocatalytic applications. *Nano. Research.* **2016,** *9* (1), 3-27.
8. Ma, Y.; Jia, Y.; Jiao, Z.; Yang, M.; Qi, Y.; Bi, Y. Hierarchical Bi_2MoO_6 nanosheet-built frameworks with excellent photocatalytic properties. *Chem. Commun.* **2015,** *51* (30), 6655-6658.
9. Dong, G.; Yang, L.; Wang, F.; Zang, L.; Wang, C. Removal of Nitric Oxide through Visible Light Photocatalysis by g-C_3N_4 Modified with Perylene Imides. *ACS. Catal.* **2016,** *6* (10), 6511-6519.
10. Li, J.; Cui, W.; Sun, Y.; Chu, Y.; Cen, W.; Dong, F. Directional electron delivery via a vertical channel between g-C_3N_4 layers promotes photocatalytic efficiency, *J. Mater. Chem. A*, **2017**, 5, 9358-9364.
11. Zhang, D.; Wen, M.; Zhang, S.; Liu, P.; Wei, Z.; Li, G.; Li, H. Au nanoparticles enhanced rutile TiO_2 nanorod bundles with high visible-light photocatalytic performance for NO oxidation. *Appl. Catal. B-Environ.* **2014,** *147* (8), 610-616.
12. Xiao, X.; Zhang, W.; Yu, J.; Sun, Y.; Zhang, Y.; Dong, F. Mechanistic understanding of ternary Ag/AgCl@La$(OH)_3$ nanorods as novel visible light plasmonic photocatalysts, *Catal. Sci. Technol.*, **2016**, 6, 5003-5010.
13. Dong, F.; Xiong, T.; Sun, Y.; Zhao, Z.; Zhou, Y.; Feng, X.; Wu, Z. A semimetal bismuth element as a direct plasmonic photocatalyst. *Chem. Commun.* **2014,** *50* (72), 10386-10389.
14. Devi, L. G.; Kavitha, R. A review on non metal ion doped titania for the photocatalytic degradation of organic pollutants under UV/solar light: Role of photogenerated charge carrier dynamics in enhancing the activity. *Appl. Catal. B-Environ.* **2013,** *140* (8), 559-587.
15. Li, Y.; Liu, M.; Chen, L. Polyoxometalate built-in conjugated microporous polymers for visible-light heterogeneous photocatalysis. *J. Mater.Chem. A.* **2017,** *5* (26), 13757-13762.
16. Zhang, Y.; Zhang, N.; Tang, Z. R.; Xu, Y. J. Graphene transforms wide band gap ZnS to a visible light photocatalyst: the new role of graphene as a macromolecular photosensitizer. *ACS Nano*, **2012,** *6* (11), 9777-9789.
17. Jiang, G. M.; Li, X. W.; Lan, M. N.; Shen, T.; Lv, X. S.; Dong, F.; Zhang, S. Monodisperse bismuth nanoparticles decorated graphitic carbonnitride: Enhanced visible-light-response photocatalytic NO removaland reaction pathway.

Appl. Catal. B : Environ. 2017, 205, 532-540.

18. Lv, S.; Li, P.; Sheng, J.; Sun, W. Synthesis of single-crystalline $BaCO_3$ nanostructures with different morphologies via a simple pvp-assisted method. *Mater. Lett.* **2007,** *61* (21), 4250-4254.

19. Dong, F.; Xiong, T.; Sun, Y.; Lu, L.; Zhang, Y.; Zhang, H.; Huang, H.; Zhou, Y.; Wu, Z. Exploring the photocatalysis mechanism on insulators. *Appl. Catal. B-Environ.* **2017,** *219* (2017), 450-458.

20. Calza, P.; Rigo, L.; Sangermano, M. Investigations of photocatalytic activities of photosensitive semiconductors dispersed into epoxy matrix. *Appl. Catal. B-Environ.* **2011,** *106* (3), 657-663.

21. Zheng, H. Q.; Guo, Y. P.; Yin, M. C.; Fan, Y. T. Synthesis, characterization of a new photosensitive compound [Ru(bpy)$_2$ (TPAD)]$(PF_6)_2$ and its application for photocatalytic hydrogen production. *Chem. Phys. Lett.* **2016,** *653* (2016), 17-23.

22. Huang, H.; He, Y.; Du, X.; Chu, P. K.; Zhang, Y. A general and facile approach to heterostructured core/shell $BiVO_4$/BiOI p-n junction: Room-temperature in situ assembly and highly boosted visible-light photocatalysis. *Acs. Sustain. Chem. Eng.* **2015,** *3* (12), 3262-3273.

23. Reddy, K. H.; Martha, S.; Parida, K. M. Fabrication of novel p-BiOI/n-$ZnTiO_3$ heterojunction for degradation of rhodamine 6G under visible light irradiation. *Inorg. Chem.* **2013,** *52* (11), 6390-401.

24. Ping, W.; Jin, W.; Ming, T.; Wang, X.; Yu, H.; Yu, J.; Wang, Y.; Ming, L. Dye-sensitization-induced visible-light reduction of graphene oxide for the enhanced TiO_2 photocatalytic performance. *Appl. Mater. Inter.* **2013,** *5* (8), 2924-2929.

25. Xu, H.; Yan, J.; Xu, Y.; Song, Y.; Li, H.; Xia, J.; Huang, C.; Wan, H. Novel visible-light-driven AgX/graphite-like C_3N_4 (x = Br, I) hybrid materials with synergistic photocatalytic activity. *Appl. Catal. B-Environ.* **2013,** *129* (2), 182-193.

26. Furthmüller, G. K. J. Efficient iterative schemes for ab initio total-energy calculations using a plane-wave basis set. *Phys. Rev. B.* **1996,** *54* (16), 11169.

27. Furthmüller, G. K. J. Efficiency of ab-initio total energy calculations for metals and semiconductors using a plane-wave basis set. *Comp. Mater. Sci.* **1996,** *6* (1), 15-50.

28. Perdew, J. P.; Burke, K.; Ernzerhof, M. *Generalized gradient approximation made simple*. Phys. Rev. Lett, 1996; Vol. 77, p 3865.

29. Blöchl, B. P. Projector augmented-wave method. *Phys. Rev. B.* **1994,** *50* (24), 17953.

30. Kresse, G. From ultrasoft pseudopotentials to the projector augmented-wave method. *Phys. Rev. B.* **1999,** *59* (3), 1758-1775.

31. Bhatia, S. K.; Myers, A. L. Optimum conditions for adsorptive storage. *Langmuir.* **2006,** *22* (4), 1688-1700.

32. Lochan, R. C.; Headgordon, M. Computational studies of molecular hydrogen binding affinities: The role of dispersion forces, electrostatics, and orbital interactions. *Phys. Chem. Chem. Phys.* **2006,** *8* (12), 1357-1370.

33. Ge, L.; Han, C.; Liu, J.; Li, Y. Enhanced visible light photocatalytic activity of novel polymeric g-C_3N_4 loaded with Ag nanoparticles. *Appl. Catal. A-Gen.* **2011,** *409* (23), 215-222.

34. Chen, L.; Yin, S. F.; Luo, S. L.; Huang, R.; Zhang, Q.; Hong, T.; Au, P. C. T. $Bi_2O_2CO_3$/BiOI photocatalysts with heterojunctions highly efficient for visible-light treatment of dye-containing wastewater. *Ind. Eng. Chem. Res.* **2012,** *51* (19), 6760-6768.

35. Hou, D.; Luo, W.; Huang, Y.; Yu, J. C.; Hu, X. Synthesis of porous $Bi_4Ti_3O_{12}$ nanofibers by electrospinning and their enhanced visible-light-driven photocatalytic properties. *Nanoscale.* **2013,** *5* (5), 2028-2035.

36. Liu, J.; Zou, S.; Xiao, L.; Fan, J. Well-dispersed bimetallic nanoparticles confined in mesoporous metal oxides and their optimized catalytic activity for nitrobenzene hydrogenation. *Catal. Sci. Technol.* **2014,** *4* (2), 441-446.

37. Ding, X.; Ho, W.; Shang, J.; Zhang, L. Self doping promoted photocatalytic removal of NO under visible light with Bi_2MoO_6: Indispensable role of superoxide ions. *Appl. Catal. B-Environ.* **2016,** *182* (2016), 316-325.

38. Zhang, W.; Zhang, Q.; Dong, F. Visible-light photocatalytic removal of NO in air over BiOX (X = Cl, Br, I) single-crystal nanoplates prepared at room temperature. *Ind. Eng. Chem. Res.* **2013,** *52* (20), 6740-6746.

39. Dong, F.; Li, Y.; Ho, W.; Zhang, H.; Fu, M.; Wu, Z. Synthesis of mesoporous polymeric carbon nitride exhibiting enhanced and durable visible light photocatalytic performance. *Chinese. Sci. Bull.* **2014,** *59* (7), 688-698.

40. Sun, Y.; Xiong, T.; Dong, F.; Huang, H.; Cen, W. Interlayer-I-doped $BiOIO_3$ nanoplates with an optimized electronic structure for efficient visible light photocatalysis. *Chem. Commun.* **2016,** *52* (53), 8243-8246.

41. Dong, F.; Lee, S. C.; Wu, Z.; Huang, Y.; Fu, M.; Ho, W. K.; Zou, S.; Wang, B. Rose-like monodisperse bismuth subcarbonate hierarchical hollow microspheres: One-pot template-free fabrication and excellent visible light photocatalytic activity and photochemical stability for NO removal in indoor air. *J. Hazard. Mater.* **2011,** *195*, 346-354.

42. Wu, J. C. S.; Cheng, Y. T. *In situ* FT-IR study of photocatalytic no reaction on photocatalysts under UV irradiation. *J. Catal.* **2006,** *237* (2), 393-404.

43. Tang, N.; Liu, Y.; Wang, H.; Wu, Z. Mechanism study of NO catalytic oxidation over $MnOx/TiO_2$ catalysts. *J. Phys. Chem. C.* **2011,** *115* (16), 8214-8220.

44. Jaan, L.; Ohlsen, J. R., *Characterization of nitrogen oxides by vibrational spectroscopy*. 2007; p 465-513.

45. Hadjiivanov, K. I. Identification of neutral and charged NxOy surface species by IR spectroscopy. *Catal. Rev.* **2000,** *42* (1-2), 71-144.

46. Cui, W.; Li, J.; Dong, F.; Sun, Y.; Jiang, G.; Cen, W.; Lee, S. C.; Wu, Z. Highly Efficient Performance and Conversion Pathway of Photocatalytic NO Oxidation on SrO-Clusters@Amorphous Carbon Nitride, *Environ. Sci. Technol.*, **201**7, 51 (18), 10682-10690.

47. Cui, W.; Li, J.; Cen, W.; Sun, Y.; Lee, S. C.; Dong, F. Steering the interlayer energy barrier and charge flow *via* bi-oriented transportation channels in $g\text{-}C_3N_4$: enhanced photocatalysis and reaction mechanism, *J. Catal.*, **2017**, 352, 351-360.

48. Xu, Y.; Schoonen, M. A. A. The absolute energy positions of conduction and valence bands of selected semiconducting minerals. *Am. Mineral.* **2000,** *85* (3-4), 543-556.

TOC Art

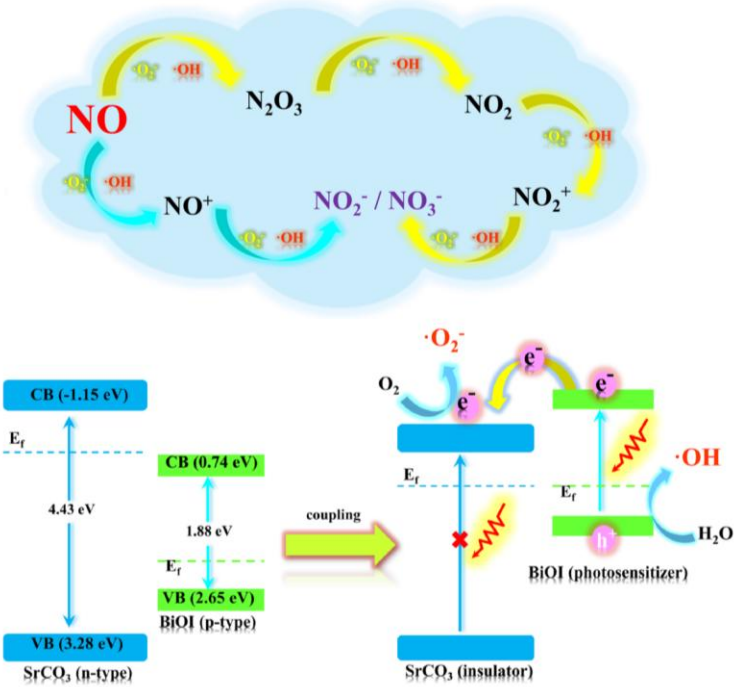
NO
N2O3
NO2
NO+
NO2- / NO3-
NO2+
·O2-
·OH
CB (-1.15 eV)
Ef
4.43 eV
VB (3.28 eV)
SrCO3 (n-type)
CB (0.74 eV)
1.88 eV
VB (2.65 eV)
BiOI (p-type)
coupling
O2
e-
h+
H2O
BiOI (photosensitizer)
SrCO3 (insulator)